Evidence for Polar Symmetry Coupling at MoS$_2$/Ferroelectric Heterointerfaces

Preprint · March 2019

CITATIONS
0

READS
194

10 authors, including:

Dawei Li
Dalian University of Technology
67 PUBLICATIONS **1,071** CITATIONS
SEE PROFILE

Xi Huang
University of Nebraska at Lincoln
62 PUBLICATIONS **1,123** CITATIONS
SEE PROFILE

Zhiyong Xiao
University of Nebraska at Lincoln
25 PUBLICATIONS **381** CITATIONS
SEE PROFILE

Hanying Chen
University of Nebraska at Lincoln
6 PUBLICATIONS **31** CITATIONS
SEE PROFILE

Evidence for Polar Symmetry Coupling at MoS_2/Ferroelectric Heterointerfaces

Dawei Li[1,4], Xi Huang[2,4], Zhiyong Xiao[1], Hanying Chen[1], Le Zhang[1], Jingfeng Song[1], Ding-Fu Shao[1], Evgeny Y. Tsymbal[1,3], Yongfeng Lu[2,3*], and Xia Hong[1,3*]

[1] Department of Physics and Astronomy, University of Nebraska-Lincoln, Lincoln, Nebraska 68588-0299, USA

[2] Department of Electrical and Computer Engineering, University of Nebraska-Lincoln, Lincoln, Nebraska 68588-0511, USA

[3] Nebraska Center for Materials and Nanoscience, University of Nebraska-Lincoln, Nebraska 68588-0298, USA

[4] These authors contributed equally: Dawei Li, Xi Huang

[*] email: X.H. (xia.hong@unl.edu); Y.L. (ylu2@unl.edu)

The complex oxide heterointerfaces[1] and van der Waals (vdW) heterostructures[2] present two versatile platforms for exploring emergent quantum phenomena and designing new functionalities. The former hosts interfacial magnetoelectric coupling,[3] gate tunable two-dimensional (2D) superconductivity[4] and topological states,[5] and polar vortices,[6] and the latter leads to the discoveries of the long sought after Hofstadter butterfly,[7-9] moiré excitons,[10-12] and correlation-driven quantum phase transitions.[13, 14] The rich opportunity offered by the synergy between complex oxides and vdW materials, however, is yet to be charted. In this work, we report the nonlinear optical signature of the polar coupling between monolayer (1L) MoS_2 and a neighboring ferroelectric oxide thin film. The interfacial second harmonic generation (SHG) response can be substantially enhanced or

almost entirely quenched by the domain walls (DWs) or polar domains in the ferroelectric. Unlike the extensively studied coupling mechanisms driven by charge, spin, and lattice,[15] this unconventional optical filtering effect is solely mediated by the interfacial polar symmetry, pointing to a new material strategy for the functional design of nanoscale reconfigurable optical applications.

Like the ferroelectrics, 1L transition metal dichalcogenides (TMDC) such as MoS_2 are non-centrosymmetric and possess polar axes. The associated functional phenomena, including piezoelectricity[16] and polar metal switching,[17] have drawn substantial research interests recently. When 2D TMDC is interfaced with a ferroelectric gate, the spontaneous ferroelectric polarization offers the unique opportunity to induce nonvolatile charge modulation in the channel.[15, 18, 19] Combining the polarization doping with nanoscale ferroelectric domain patterning further allows local tuning of the electronic[19, 20] and optical properties[21] of the vdW layer. Beyond the charge mediated interfacial coupling, the polar alignment between TMDC and ferroelectric has never been explored to date. In this work, we report the nonlinear optical evidence for the direct polar symmetry coupling at the interface between 1L MoS_2 and ferroelectric $PbZr_{0.2}Ti_{0.8}O_3$ (PZT). The heterostructure exhibits either strong enhancement or substantial quenching of the reflected SHG response at the ferroelectric DWs. In sharp contrast, the transmitted SHG signal is sensitively tuned by the out-of-plane ferroelectric domain rather than the DW. The distinct SHG responses reveal the intricate coupling of the polar axis of MoS_2 with either the chiral rotation of the surface dipole at the DWs or the out-of-plane polarization of PZT, which is modeled via density functional theory (DFT) calculations.

Figure 1a shows the experimental setup for the SHG imaging of the MoS_2-ferroelectric heterostructure. Monolayer MoS_2 flakes were mechanically exfoliated from bulk crystals on Gel-Films and identified via the frequency difference Δ between the E_{2g}^1 and A_{1g} modes in the Raman spectrum (Fig. 1b). Selected MoS_2 flakes were then transferred on top of a 50 nm epitaxial PZT thin film above a region patterned with a series of square domains with alternating down (P_{down}) and up (P_{up}) polarization. Figures 1c and 1d show the piezoresponse force microscopy (PFM) phase images of the domain patterns before and after the MoS_2 transfer, respectively. The crystalline orientation of MoS_2 was identified while being on the Gel-Film by the polar angle measurement of the SHG response (Supplementary Information). During transfer, the zigzag axis of MoS_2 was aligned with the horizontal DWs. Figure 1e compares the photoluminescence (PL) spectra of MoS_2 obtained from the regions on the P_{up} and P_{down} domains, with the corresponding PL mapping shown in Fig. 1f. While there is no change in the peak position, both the PL intensity and width exhibit strong dependence on the PZT polarization states. The region above the P_{up} domain exhibits higher PL intensity, narrower peak width, and enhanced trion/neutral exciton populations (Supplementary Information), which are consistent with a higher electron doping.[21]

Monolayer MoS_2 exhibits strong nonlinear optical responses, such as SHG[20, 22-24] and sum-frequency generation,[20, 24] due to the lack of inversion symmetry. For normal incident light (800 nm center wavelength), we observed strong SHG signals (λ ~400 nm) from the 1L MoS_2 flakes on Gel-Films conforming to the rotational symmetry of the lattice in both the reflection and transmission modes (Supplementary Information). For the PZT films, as the incident light is along the polar axis (*c*-axis), there is no SHG response on the uniformly polarized domains, as shown in the SHG mapping image (Fig. 2a). Prominent SHG signals have only been observed at

the DWs, consistent with previous reports on PZT[25, 26] thin films, which suggests the existence of an in-plane polarization ($p_{\parallel}$) facilitated by the DW. To determine the orientation of $p_{\parallel}$, we performed SHG imaging at different analyzer orientations. As shown in Figs. 2b-d, the SHG response can only be detected when the analyzer can be projected along the direction perpendicular to the DWs. This means that $p_{\parallel}$ is residing in a plane normal to the DW, similar to the Néel-type chiral DW.[25] In bulk PZT, the DWs are known to be at the unit cell scale, and such chiral DW is not energetically favorable.[27] Continuous rotation of local dipoles, however, can be stabilized at the surface of PZT thin films by depolarization field,[28] resulting a net lateral polarization. For both MoS_2 on Gel-Films and bare PZT, the SHG signals in the transmitted mode exhibit qualitatively similar behaviors as in the reflected mode (Supplementary Information).

We then mapped the SHG response of the lL MoS_2/PZT heterostructure. Figure 2e shows the reflected SHG mapping taken on the same domain structure in PZT with the lL MoS_2 transferred on top. The imaging condition is similar to that used in Fig. 2a, *i.e.*, with horizontal incident light polarization (zigzag axis of MoS_2) and no analyzer applied. For MoS_2 on uniformly polarized P_{up} and P_{down} domains, as expected, the SHG intensity reaches maximum at this light polarization angle.[23] At the DWs, however, MoS_2 produces a filtering effect for the reflected SHG that not only selects the light polarization, similar to that of a vertical analyzer (Fig. 2b), but also the DW chirality. Along the vertical DWs, the SHG signal is at a similar level to those on the P_{up} and P_{down} domains. This is in sharp contrast to those observed on bare PZT, where the vertical DWs have similar intensity as those from the horizontal DWs (Fig. 2a), clearly showing that the interfacial SHG signal is not a simple summation of the signal strength from each constituent layer. The horizontal DWs, more surprisingly, exhibit alternating enhancement and suppression

of the SHG signals. At the set of DWs labelled as 1, 3, and 5, the SHG response is more than two times of background signal. At the other set of DWs (labelled as 2, 4, and 6), the SHG response is substantially quenched. In Fig. 2e, the MoS_2 flake shows several cracked regions resulting from the transfer, exposing the bare PZT underneath. The fact that the SHG intensity at the even-numbered DWs are comparable to these regions indicates that the emission from MoS_2 is close to be entirely canceled by the presence of these DWs.

Figures 2f-h show the SHG mapping with an analyzer applied at the same angles φ as in Figs. 2b-c, respectively. For a vertical analyzer (Fig. 2f, $\varphi = 90°$), the image shows qualitatively similar SHG behaviors as in Fig. 2e, conforming that the signals at the DWs are linearly polarized to the vertical direction. At $\varphi = 45°$, even though the intensity of the SHG signal is significantly suppressed for both the domain and DW regions, the relative relation between them remains the same (Fig. 2g). Only when the SHG signal of MoS_2 is fully quenched by a horizontal analyzer (along the zigzag axis of MoS_2) does the signal from the vertical DWs of PZT become appreciable (Fig. 2h).

The alternating enhanced and suppressed SHG signals can be well correlated to the in-plane polar symmetry of the DWs. A clear difference between the odd- and even-numbered DWs is the arrangement of the domains that they separate. The odd DWs are accompanied with top P_{up} and bottom P_{down} domains, opposite to the distribution for the even DWs. To conform to the bulk polarization change, the surface polarization at the vicinities of the odd and even DWs is expected to have opposite chirality, with the corresponding $\vec{p}_{\parallel}$ in opposite directions (Fig. 3a). The orientation of $\vec{p}_{\parallel}$ itself does not have an impact on the intensity of the SHG response ($I \propto \left|\vec{E}\right|^2$), as clearly shown for bare PZT in Fig. 2a. The presence of a 1L MoS_2 on top, however,

modifies the polar symmetry at the interface. The polar, armchair direction of the MoS_2 flake is along the vertical direction, which is either parallel or anti-parallel to $\vec{p}_{\parallel}$ for the parallel DWs depending on the charity. The enhanced or suppressed SHG response can thus be attributed to the coupling of the polar axis of MoS_2 ($\vec{P}_{MoS_2}$) with the in-plane polarization at the PZT DWs ($\vec{P}_{DW}$).

To examine the feasibility of this scenario, we exploited a phenomenological model to estimate the net in-plane polarization produced by a triangle-shaped flux-closure domain structure (Fig. 3a), which hosts continuous electric dipole rotations above a 180° DW.[28] The bulk values of the out-of-plane (P_{out}) and in-plane (P_{in}) polarization were calculated via DFT within the local density approximation (Supplementary Information), which yields $P_{out} = 78.1\ \mu C\ cm^{-2} = 0.049\ e\ \text{Å}^{-2}$ and $P_{in} = 59.1\ \mu C\ cm^{-2} = 0.037\ e\ \text{Å}^{-2}$. The polarization at point (x, z) inside this triangular area can be projected to the in-plane $P_{\parallel}(x, z)$ and out-plane $P_{\perp}(x, z)$ components. The net in-plane dipole moment can then be estimated by integrating $P_{\parallel}(x, z)$ over the volume of the flux-closure domain V_{PZT}. We thus deduced the in-plane dipole density as:

$$p_{\parallel} = \frac{\int P_{\parallel}(x,z) dV_{PZT}}{l} = \iint P_{\parallel}(x, z) dx dz = \frac{wh}{4} \cdot P_{in} = 6.92\ e. \qquad (1)$$

Here we assumed the maximum width w and depth h of the triangle domain to be 2.5 nm and 3 nm based on previous experimental observations,[28] and l is the lateral extension of the DW.

We then considered the polar property of 1L H-MoS_2, which belongs to the D_{3h} point group. The polar displacement in the unit cell can generate three equal polarization along those three polar directions, leading to zero net polarization. However, when one of the polar axis is coupled

to a neighboring dipole, the rotational symmetry is lifted. Using DFT, we estimated the polarization of MoS_2 along one polar direction to be $P_{MoS_2} = 85.5\ \mu C\ cm^{-2}$ (Supplementary Information). Using the thickness of 1L MoS_2 of $h_1 = 3.11$ Å, we obtained the dipole moment per unit length for the area above the flux-closure DW in PZT (Fig. 3b):

$$p_{MoS_2} = P_{MoS_2} \times h_1 \times w = 6.65 \times 10^{-19}\text{C} \approx 4.15\ \text{e}, \qquad (2)$$

which is on the same order of $p_{\parallel}$ estimated for the DWs in PZT (Eq. 1). This simple model thus captures the major features of our observation. When one of the polar axes of MoS_2 is aligned with the in-plane polarization of PZT at the DW regions, as for the odd DWs, the interfacial dipole field is close to be doubled, leading to significantly enhanced SHG response that is linearly polarized along the polar axis. For the anti-aligned even DWs, where these two dipole fields cancel each other, the SHG signal is strongly suppressed. For the vertical DWs, on the other hand, $p_{\parallel}$ is not coupled to any of the polar axes of MoS_2. The SHG responses of PZT and MoS_2 remain to be independent, and we only observe the weak SHG from PZT that is filtered by the MoS_2 top layer.

To further test the proposed scenario based on the interfacial polar coupling between MoS_2 and the DW, we exploited PFM to create square domains on PZT with different DW stacking angles (θ) with the same MoS_2 top layer. Figure 3c shows the PFM phase image of four square-shaped domain structures written at different scanning directions, with $\theta = 0°, 15°, 30°$, and $45°$ relative to the *x*-axis (zigzag axis of MoS_2). For bare PZT, the SHG response is uniform at all DW regions, independent of their orientations (Fig. 3d). We then transferred a lL MoS_2 flake on top of this area, covering all four domain structures. As shown in Fig. 3e, without an analyzer, the stacking angle between MoS_2 and DW has a clear impact on

the reflected SHG intensity, suggesting that the top MoS_2 layer acts as an unconventional light polarizer. We then exploited a phenomenological model to simulate the overall SHG response for each of these DWs, considering the full dielectric tensors for both PZT and MoS_2 (Supplementary Information). To simplify the calculation, we assumed that the maximum SHG intensities from MoS_2 and flux-closure domain of PZT are the same, which is reasonable given their closely matched dipole moments. Figure 3f shows the simulated SHG results, which is in striking agreement with the experimental SHG images for different stacking angles, yielding strong support to the polar alignment model.

For the stand-alone MoS_2 and PZT domains, we observed similar SHG responses in the reflection and transmission modes. Interestingly, the hybrid structure reveals qualitatively different dependences on the ferroelectric polarization in these two detection modes. Figure 4a displays the transmitted SHG image of the same domain structure as in Fig. 2e, which exhibits a clear signal contrast between the P_{up} and P_{down} domains, rather than at the DWs. Only when a horizontal analyzer is applied does the SHG signal for the vertical DWs become appreciable (Fig. 4b), similar to that observed in the reflected mode (Fig. 2h). We also note that the relative strength of the SHG intensity between the regions of the P_{up} and P_{down} domains depends on the polarizer angle (Fig. 4c). Figure 4d shows the cross-sectional SHG signal profiles for the same region in both transmission (Fig. 4a) and reflection (Fig. 2e) modes. The signals are normalized to the intensity difference between the even (I_{even}) and odd (I_{odd}) horizontal DWs, defined as $(I - I_{even})/(I_{odd} - I_{even})$, which clearly illustrate the signal contrast either tailored by the uniformly polarized domains or the DWs, respectively.

Such ferroelectric polarization-dependent SHG response at the MoS_2-PZT interfaces indicates that the out-of-plane bulk polarization of PZT can also couple to the polar axis of MoS_2. The polarization at 1L MoS_2/PZT interfaces can thus be expressed as the superposition of the in-plane polarization of MoS_2 ($\vec{P}_{MoS_2}$) and out-of-plane polarization of PZT ($\vec{P}_{out}$): $\vec{P}_{interface} = \vec{P}_{MoS_2} + \vec{P}_{out}$. The net dipole moment, which defines the polarization of the excited SHG signal, is tilted from the surface normal. As illustrated in Fig. 4e, the propagation of the corresponding electromagnetic signal $\vec{E}_{2\omega}$ is perpendiculare to $\vec{P}_{interface}$, making a large angle $\theta_{air} = arctan\left(P_{MoS_2}/P_{out}\right) \approx 48°$ with respect to the normal axis, or the detector direction (Fig. 1a). This scenario well explains why the SHG signal from $\vec{P}_{interface}$ is absent in the reflected SHG image. Its strong presence in the transmitted signal, on the other hand, can be accounted for by the different dielectric environments for light propagation in these two detection schemes. While the reflected light travels through air, the transmitted light is actually focused through PZT, whose high dielectric constant would alter the propagation direction. For the PZT films, the dielectric constant κ is about 100,[29] yielding a refractive index $n_{PZT} = \sqrt{\kappa} \approx 10$. Using Fresnel's equation: $\sin\theta_{air} \cdot n_{air} = \sin\theta_{PZT} \cdot n_{PZT}$ and assuming the refractive index of air $n_{air} \approx 1$, we estimated the propagating angle of the transmitted signal to be $\theta_{PZT} \approx 4°$, closely aligned to the normal axis, which well explains the strong SHG intensity at the uniformly polarized domain regions. As the SHG intensities from the P_{up} and P_{down} domains depend sensitively on the light polarization and can reverse the relative strength (Figs. 4a and 4c), the difference is likely phase-related rather than due to the doping difference, and may originate from the polarization-dependent surface reconstruction in PZT thin films.[30]

In summary, we report an interface-driven nonlinear optical filtering effect in lL MoS_2/ferroelectric heterostructures. The SHG signal is solely mediated by the interfacial polar symmetry, and exhibit distinct tailoring effect in the reflection and transmission modes. Our study points to a new material platform for functional design of novel interfacial optical response via ferroelectric domain patterning, paving the way for achieving nanoscale electrically programmable optical applications.

Acknowledgements

We thank Anthony Starace and Ziliang Ye for helpful discussions, and Chengyiran Wei and Kun Wang for technical assistance. This work was primarily supported by the U.S. Department of Energy (DOE), Office of Science, Basic Energy Sciences (BES), under Award No. DE-SC0016153. Additional support is provided by the NSF Nebraska Materials Research Science and Engineering Center (MRSEC) Grant No. DMR-1420645 (PZT growth and theoretical modeling). YL acknowledges the support from NSF Award No. CMMI 1826392 and ONR Award No. N00014-15-C-0087. The research was performed in part in the Nebraska Nanoscale Facility: National Nanotechnology Coordinated Infrastructure and the Nebraska Center for Materials and Nanoscience, which are supported by the National Science Foundation under Award ECCS: 1542182, and the Nebraska Research Initiative.

Author contributions

X. Hong, D.L., and Z.X. conceived the project and designed the experiments. X. Hong supervised the project. L.Z. prepared the PZT thin films. J.S. and D.L. carried out the surface and structural characterizations of PZT. Z.X., D.L., and H.C. prepared the MoS_2/PZT

heterostructures. X. Huang, D.L., and Y.L. contributed to the Raman, PL, and SHG studies. D.L. and Z.X. carried out the PFM studies. D.S. and E.T. performed theoretical modeling of the polar states. D.L. and X. Hong wrote the manuscript. All authors discussed the results and contributed to the manuscript preparation.

Competing interests

The authors declare no competing interests.

Additional information

Correspondence and request for materials should be addressed to Xia Hong and Yongfeng Lu.

Methods

Preparation and characterization of epitaxial PZT. We deposited epitaxial PZT on $La_{0.67}Sr_{0.33}MnO_3$ (LSMO) buffered (001) $SrTiO_3$ substrates via off-axis radio frequency magnetron sputtering. LSMO (10 nm) films were first grown at 650 ºC in 120 mTorr process gas composed of Ar and O_2 (ratio 2:1). The PZT layers (50 nm) were deposited *in situ* at 490 ºC in 150 mTorr process gas ($Ar:O_2$ = 2:1). The PZT films is *c*-axis oriented with out-of-plane polar axis (Supplementary Information). Atomic force microscopy (AFM) images show smooth surface morphology with 2-3 Å surface roughness.

Preparation of MoS_2/PZT heterostructure. 1L MoS_2 flakes were mechanically exfoliated on elastomeric films (Gel-Film® WF×4 1.5mil from Gel-Pak) from bulk single crystals. Selected flakes were transferred on top of the patterned domain structures using an all-dry transfer technique. The Gel-Film with exfoliated MoS_2 was flipped upside down and anchored with a high-precision XYZ manipulator. The PZT sample was placed on a rotatable hot plate. We then aligned the MoS_2 sample with the patterned domains under an optical microscope with sub-micron precision and less than 1° rotation. The temperature was kept at ~50°C during transfer.

PFM measurements. The PFM studies were carried out using a Bruker Multimode 8 AFM. The measurements were performed in contact mode using conductive PtIr-coated tips (SCM-PIT, spring constant k of 1-5 Nm^{-1}, resonant frequency f_o of 60-100 kHz). The coercive voltage of the PZT films is about +2 V (-3 V) for the P_{down} (P_{up}) state (Supplementary Information). For domain writing, a ±7 V DC bias was applied to the AFM tip while scanning and the LSMO bottom layer was grounded. For imaging, an AC voltage of 0.5 V was applied at close to the contact resonant frequency.

Raman and PL measurements. Raman and PL measurements were performed on a micro-Raman system (Renishaw InVia plus, Renishaw) at room temperature. An Ar+ laser of about 200 μW was focused to a 1 μm beam spot on the sample at normal incidence. Both Raman and PL spectra were collected in reflection mode through a 50× objective lens with an accumulation time of 10 s.

SHG measurements. The experimental setup for SHG imaging is shown in Fig. 1a. The laser source for SHG microscopy is provided by a mode-locked Ti:Sapphire fs laser (MaiTai DeepSee HP, SpectraPhysics) with a fixed wavelength of 800 nm, duration of 100 fs, total output power of 2.95 W, and repetition rate of 80 MHz. The laser beam passed a polarizer, and then was guided by mirrors into a laser scanning microscope (LSM). The laser power before entering the LSM was tuned to ~30 mW by a variable attenuator. In the LSM, the laser beam was linearly focused onto the sample surfaces using a water-immersed Olympus objective lens (1.05 NA, 25×). To avoid water contact, a 0.17 mm thin glass cover slide was placed above the sample surface, forming a thin air gap between the sample and the cover slide. The SHG signals were collected in both reflection and transmission geometries by photomultiplier detectors (PMTs). The band-pass filter used for SHG imaging is a Semrock FF01-390/40 (T_{avg} > 93% @ 370-410 nm, center wavelength of ~ 390 nm, and bandwidth of ~ 40 nm). The analyzer is a Thorlab LPVISE100-A with operating wavelength range of 400-700 nm. Before SHG signals enter the PMTs, the excitation laser beam was filtered out by an IR cut filter (OD >4 @ 692-1100 nm).

References

1. Hwang, H.Y. et al. Emergent phenomena at oxide interfaces. *Nature Materials* **11**, 103-113 (2012).
2. Geim, A.K. & Grigorieva, I.V. Van der Waals heterostructures. *Nature* **499**, 419-425 (2013).
3. Vaz, C.A.F., Hoffman, J., Anh, C.H. & Ramesh, R. Magnetoelectric Coupling Effects in Multiferroic Complex Oxide Composite Structures. *Adv. Mater.* **22**, 2900-2918 (2010).
4. Caviglia, A.D. et al. Electric field control of the $LaAlO_3/SrTiO_3$ interface ground state. *Nature* **456**, 624-627 (2008).
5. Ohuchi, Y. et al. Electric-field control of anomalous and topological Hall effects in oxide bilayer thin films. *Nature Communications* **9**, 213 (2018).
6. Yadav, A.K. et al. Observation of polar vortices in oxide superlattices. *Nature* **530**, 198 (2016).
7. Dean, C.R. et al. Hofstadter's butterfly and the fractal quantum Hall effect in moire superlattices. *Nature* **497**, 598-602 (2013).
8. Ponomarenko, L.A. et al. Cloning of Dirac fermions in graphene superlattices. *Nature* **497**, 594-597 (2013).
9. Hunt, B. et al. Massive Dirac Fermions and Hofstadter Butterfly in a van der Waals Heterostructure. *Science* **340**, 1427-1430 (2013).
10. Jin, C. et al. Observation of moiré excitons in WSe_2/WS_2 heterostructure superlattices. *Nature* (2019).
11. Seyler, K.L. et al. Signatures of moiré-trapped valley excitons in $MoSe_2/WSe_2$ heterobilayers. *Nature* (2019).
12. Tran, K. et al. Evidence for moiré excitons in van der Waals heterostructures. *Nature* (2019).
13. Cao, Y. et al. Correlated insulator behaviour at half-filling in magic-angle graphene superlattices. *Nature* **556**, 80 (2018).
14. Cao, Y. et al. Unconventional superconductivity in magic-angle graphene superlattices. *Nature* **556**, 43 (2018).
15. Hong, X. Emerging ferroelectric transistors with nanoscale channel materials: the possibilities, the limitations. *Journal of Physics: Condensed Matter* **28**, 103003 (2016).
16. Wu, W.Z. et al. Piezoelectricity of single-atomic-layer MoS_2 for energy conversion and piezotronics. *Nature* **514**, 470 (2014).
17. Fei, Z.Y. et al. Ferroelectric switching of a two-dimensional metal. *Nature* **560**, 336 (2018).
18. Lipatov, A., Sharma, P., Gruverman, A. & Sinitskii, A. Optoelectrical Molybdenum Disulfide (MoS_2)-Ferroelectric Memories. *ACS Nano* **9**, 8089-8098 (2015).
19. Xiao, Z., Song, J., Ferry, D.K., Ducharme, S. & Hong, X. Ferroelectric-Domain-Patterning-Controlled Schottky Junction State in Monolayer MoS_2. *Physical Review Letters* **118**, 236801 (2017).
20. Li, D. et al. A Facile Space-Confined Solid-Phase Sulfurization Strategy for Growth of High-Quality Ultrathin Molybdenum Disulfide Single Crystals. *Nano Letters* **18**, 2021-2032 (2018).
21. Li, C.H., McCreary, K.M. & Jonker, B.T. Spatial Control of Photoluminescence at Room Temperature by Ferroelectric Domains in Monolayer WS_2/PZT Hybrid Structures. *ACS Omega* **1**, 1075-1080 (2016).

22. Kumar, N. et al. Second harmonic microscopy of monolayer MoS_2. *Physical Review B* **87**, 161403 (2013).
23. Li, Y.L. et al. Probing Symmetry Properties of Few-Layer MoS_2 and h-BN by Optical Second-Harmonic Generation. *Nano Letters* **13**, 3329-3333 (2013).
24. Li, D. et al. Multimodal Nonlinear Optical Imaging of MoS_2 and MoS_2-Based van der Waals Heterostructures. *ACS Nano* **10**, 3766-3775 (2016).
25. Cherifi-Hertel, S. et al. Non-Ising and chiral ferroelectric domain walls revealed by nonlinear optical microscopy. *Nature communications* **8**, 15768 (2017).
26. De Luca, G. et al. Domain wall architecture in tetragonal ferroelectric thin films. *Advanced Materials* **29**, 1605145 (2017).
27. Meyer, B. & Vanderbilt, D. Ab initio study of ferroelectric domain walls in $PbTiO_3$. *Physical Review B* **65**, 104111 (2002).
28. Jia, C.-L., Urban, K.W., Alexe, M., Hesse, D. & Vrejoiu, I. Direct Observation of Continuous Electric Dipole Rotation in Flux-Closure Domains in Ferroelectric $Pb(Zr,Ti)O_3$. *Science* **331**, 1420-1423 (2011).
29. Hong, X., Posadas, A., Zou, K., Ahn, C.H. & Zhu, J. High Mobility Few Layer Graphene Field Effect Transistors Fabricated on Epitaxial Ferroelectric Gate Oxides. *Physical Review Letters* **102**, 136808 (2009).
30. Gao, P. et al. Atomic mechanism of polarization-controlled surface reconstruction in ferroelectric thin films. *Nature Communications* **7**, 11318 (2016).

Figure 1

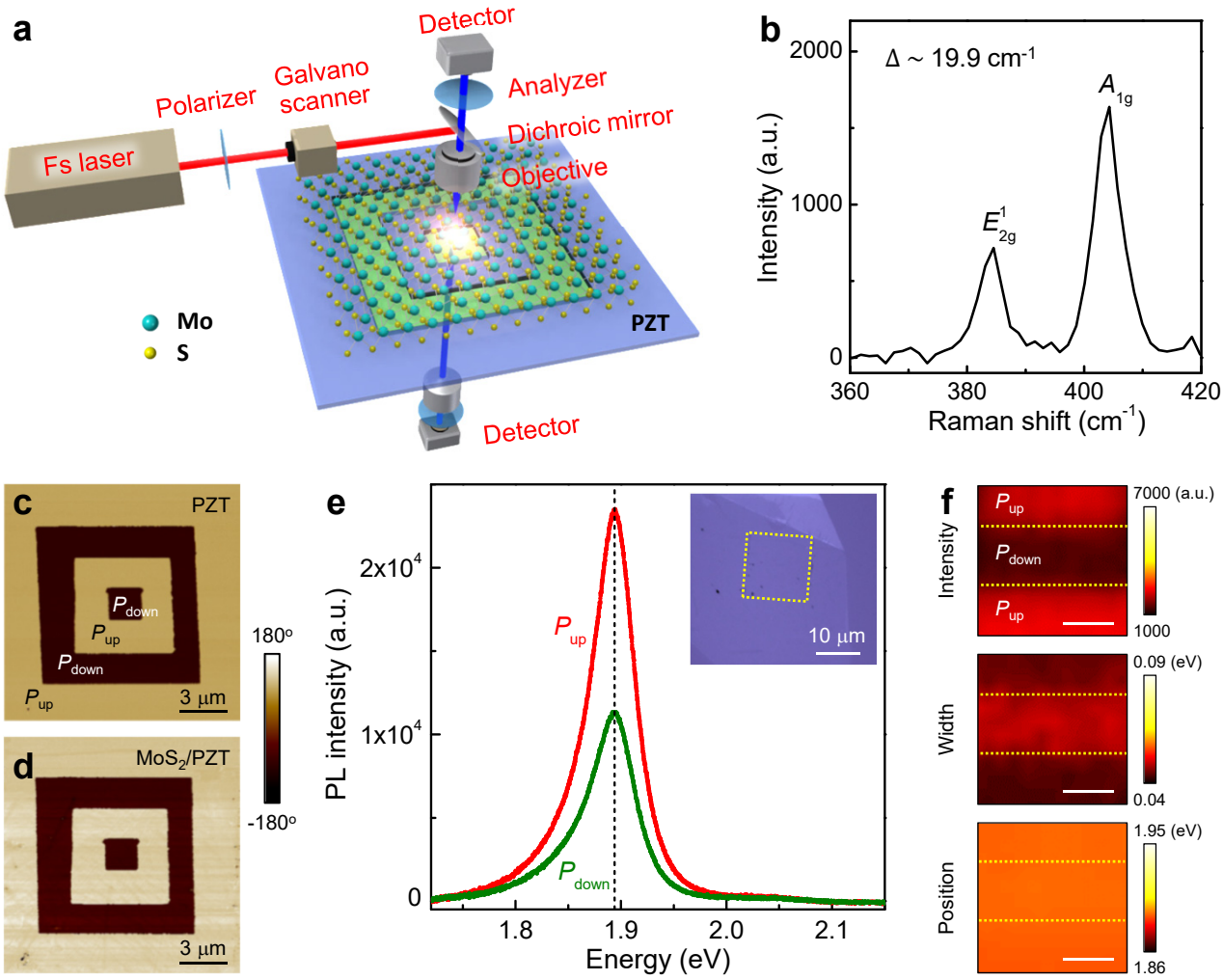

Fig. 1 | Characterization of 1L MoS_2/PZT heterostructures. a, Schematic of the SHG experimental setup. **b**, Raman spectrum of a 1L MoS_2 flake on gel film showing E^1_{2g} mode at 384.0 cm^{-1} and A_{1g} mode at 403.9 cm^{-1}. **c-d**, PFM phase images of **(c)** square domains written on a PZT film, and **(d)** the same region with a 1L MoS_2 transferred on top. **e**, Room temperature PL spectra of the 1L MoS_2 on the P_{up} and P_{down} domains shown in **d**. The region is outlined in the optical image of the sample (**inset**). **f**, PL mapping of the peak intensity (upper), width (middle), and position (lower) on a 1L MoS_2/PZT sample in a region with both P_{up} and P_{down} domains. The dotted lines mark the DW positions. The scale bars are 2 μm.

Figure 2

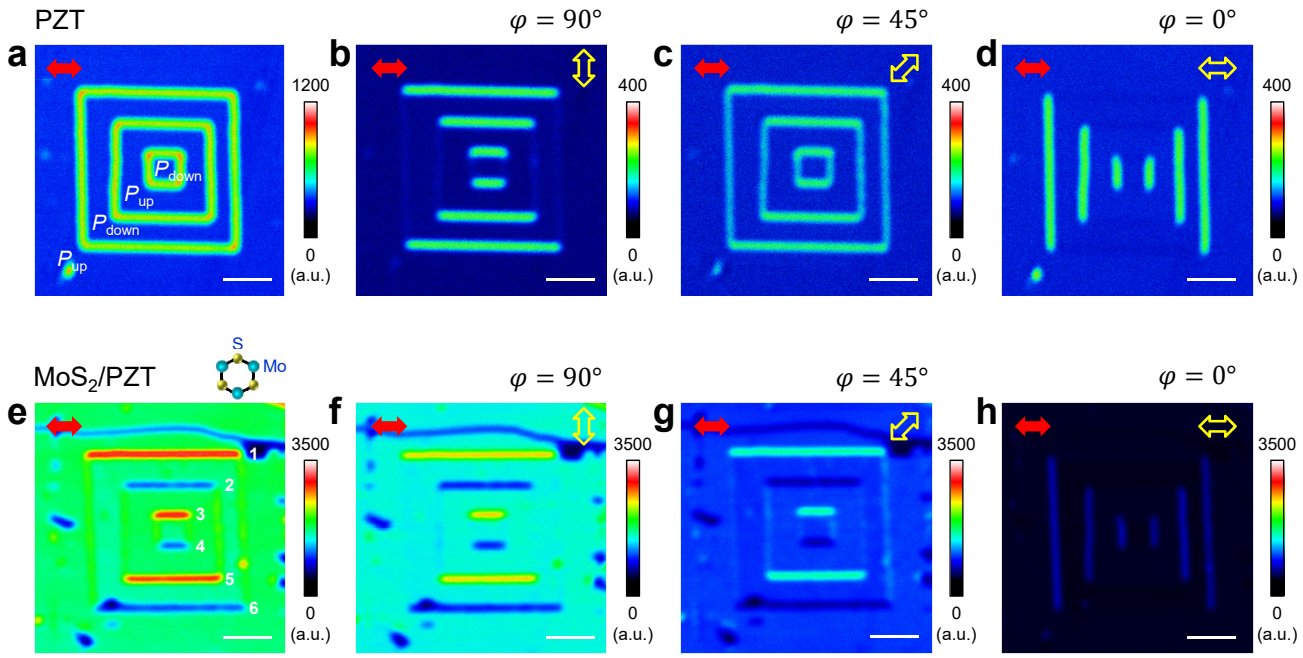

Fig. 2 | Reflected SHG response of domains on PZT with and without MoS_2 top layer. a-d, SHG mapping of the square domains shown in Fig. 1c taken **a,** with no analyzer applied, and **b-d,** with an analyzer applied at different angles φ (yellow open arrows) with respect to the incident light polarization (red solid arrows). **e-h,** SHG mapping of the same domain structure with a 1L MoS_2 flake transferred on top taken with the same polarizer and analyzer settings as in **a-d**, respectively. The crystalline orientation of MoS_2 is shown in **e** inset. The scale bars are 3 μm.

Figure 3

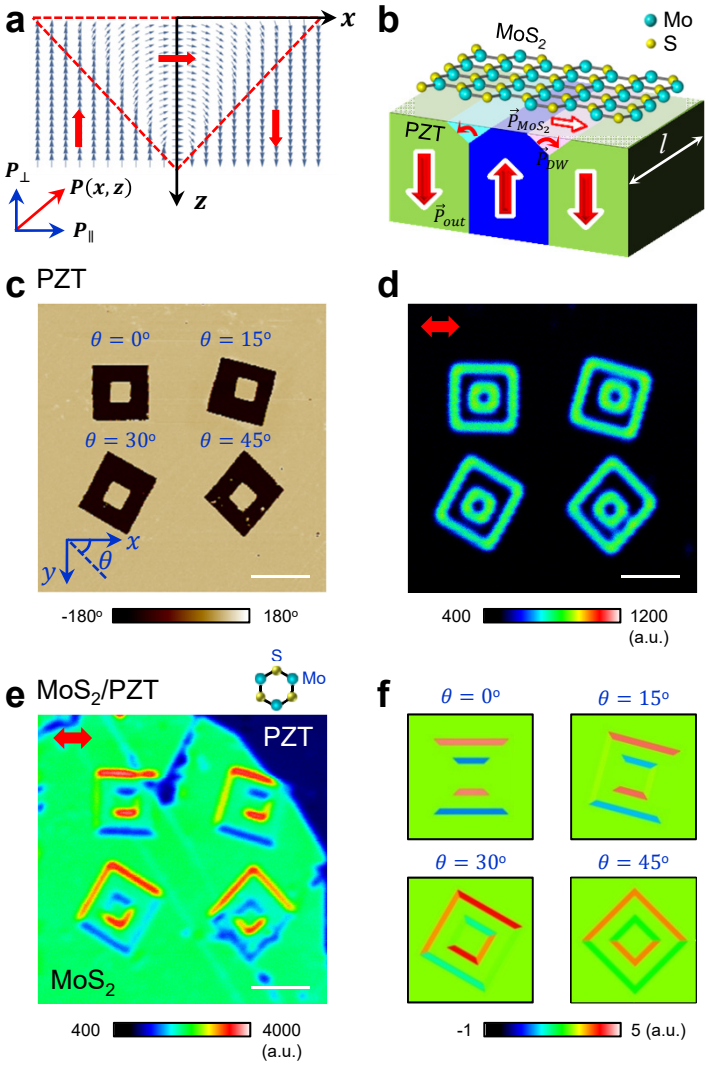

Fig. 3 | Effect of polar alignment on the reflected SHG response. a-b, Schematics of **a,** a flux-closure domain (boundary outlined by red dashed lines) at PZT surface above a 180° DW, and **b,** the polar alignment at the 1L MoS_2/PZT interface. The arrows mark the local polarization orientation. **c,** PFM phase image of square domains written on PZT along different angle θ, with the corresponding SHG images taken **d,** before and **e,** after a 1L MoS_2 transferred on top. The crystalline orientation of MoS_2 is shown in **e** inset. The red arrows mark the incident light polarization. There is no analyzer applied. The scale bars are 3 μm. **f,** Simulated SHG amplitude at 1L MoS_2/PZT interface for the same domain structures in **c-e**.

Figure 4

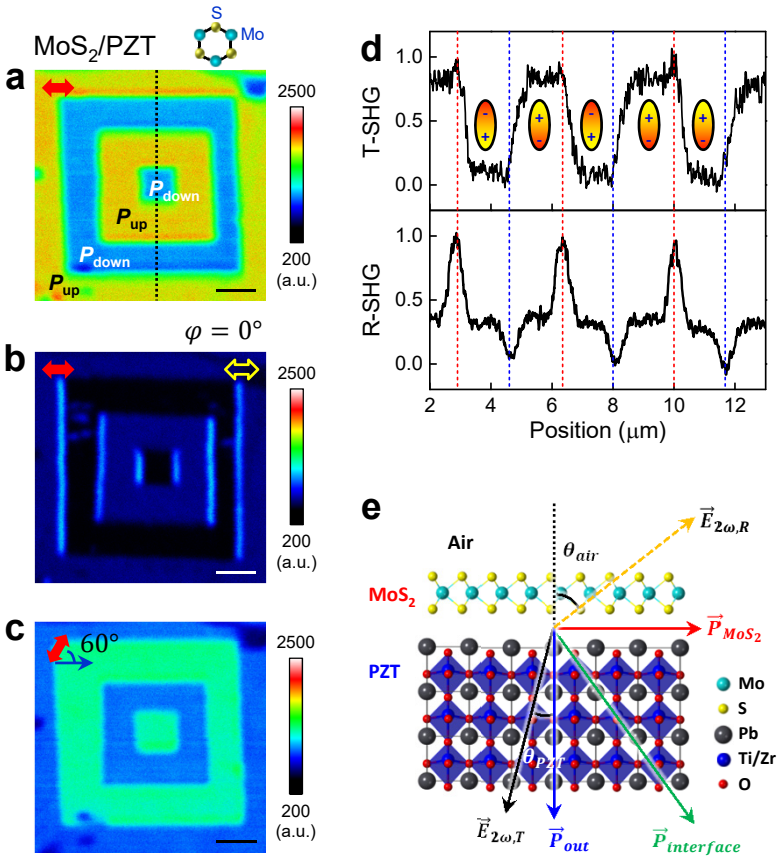

Fig. 4 | Transmitted SHG response of 1L MoS_2/PZT interface. a-c, SHG mapping in transmission mode of the same MoS_2/PZT sample shown in **Fig. 2** taken **a** and **c**, with no analyzer applied, and **b**, with a horizontal analyzer applied (yellow open arrow). The red solid arrows mark the incident light polarization. The crystalline orientation of MoS_2 is indicated in the top inset in **a**. The scale bars are 2 μm. **d,** Normalized SHG intensity profiles obtained in the transmission (T-SHG) and reflection (R-SHG) modes along the black dotted line in **a**. The dashed lines serve as the guide to the eye. **e**, Schematic view showing the interfacial polarization coupling. The resulting SHG signal propagates through air in the reflection mode $\vec{E}_{2\omega,R}$ (dashed orange arrow) and through PZT in the transmission mode $\vec{E}_{2\omega,T}$ (solid black arrow).